 doi:10.20944/preprints202208.0426.v1

Article

Multi-View and Shift Rasterization Algorithm (MVSR) for Effective Identification of Ground in Dense Point Clouds

Martin Štroner *, Rudolf Urban and Lenka Línková

Department of Special Geodesy, Faculty of Civil Engineering, Czech Technical University in Prague, Thákurova 7, 166 29 Prague, Czech Republic; martin.stroner@fsv.cvut.cz (M. Š.);
rudolf.urban@fsv.cvut.cz (R. U.)
lenka.linkova@fsv.cvut.cz (L. L)
* Correspondence: martin.stroner@fsv.cvcut.cz

Abstract: With the ever-increasing popularity of unmanned aerial vehicles and other platforms providing dense point clouds, filters for identification of ground points in such dense clouds are needed. Many filters have been proposed and are widely used, usually based on the determination of an original surface approximation and subsequent identification of points within a predefined distance from such surface. We present a new filter, Multi-view and shift rasterization algorithm (MVSR) is based on a different principle, i.e., on the identification of just the lowest points in individual grid cells, shifting the grid along both planar axis and subsequent tilting of the entire grid. The principle is presented in detail and compared both visually and numerically to other commonly used ground filters (PMF, SMRF, CSF, ATIN) on three sites with different ruggedness and vegetation density. Visually, the MVSR filter showed the smoothest and thinnest ground profiles, with ATIN the only filter performing comparably. The same was confirmed when comparing ground filtered by other filters with the MVSR-based surface. The goodness of fit with the original cloud is demonstrated by the root mean square deviations (RMSD) of the points from the original cloud found below the MVSR-generated surface (ranging, depending on site, between 0.6-2.5 cm). The MVSR filter performed outstandingly at all sites, identifying the ground points with great accuracy while filtering out the maximum of vegetation/above-ground points. The filter dilutes the cloud somewhat; in such dense point clouds, however, this can be perceived rather as a benefit than as a disadvantage.

Keywords: Point cloud; Ground filtering; Classification

1. Introduction

Advances in the current measurement techniques have made it possible to routinely use advanced methods of bulk data collection, which found application not only in the technical and engineering fields. Acquisition of such data is possible using 3D scanners (lidars) or photogrammetric systems (usually based on the Structure from Motion method), mounted on a static platform [1], on standard ground- or airborne platforms such as UAV, [2–4], or even on an airship [5]. Such measurement systems result in point clouds of, typically, hundreds of millions to billions of points. Such large-scale data cannot be processed without at least semi-automated tools. Since at least some parts of the area of interest are massively oversampled, the initial processing phase usually involves dilution to the necessary (while usable) density, which is followed by the extraction of data needed for further processing. These activities typically include vegetation removal and, thus, extraction of points characterizing the objects of interest – be it the terrain, building structures, or anything else.

Such approaches to capturing the reality are being employed in many fields, from reality modeling for identification of historical monuments [6], infrastructure mapping [7], mapping of open-pit mines [8], monitoring of changes during mining [9], coastline

 doi:10.20944/preprints202208.0426.v1

mapping [10], intertidal reef analysis [11], measurements for the purposes of building reconstruction [12], earthworks volume calculations [13], archaeological documentation [14], etc. Often, the data are processed to produce a general [15] or specialized [16] Digital Terrain Model (DTM).

1.1 Current ground filtering approaches

Vegetation removal, or, more generally, identification of cloud points representing the terrain (ground) is a specific activity, for which a considerable number of filters (algorithms and their implementations in software) have been developed. They can be classified into slope-based filters, interpolation-based, morphology-based, segmentation-based, statistics-based, and hybrid filters, machine learning, and other unclassified filters.

Slope-based filters work with the assumption that the terrain does not change abruptly; these methods determine the slopes in the vicinity of a point and compare the results with a maximum preset slope. These methods work fine in flat terrain but they are less effective in a rugged or forested landscape (e. g. [17–19]). Interpolation-based filters first select the "seed" ground points from the point cloud using a window size slightly exceeding the size of the biggest object in the area. Then, an approximation of the surface among such points is created and, using a threshold comparing the distance of remaining points in the cloud from this surface, add additional points (densify the cloud) (e.g. [20–22]). Morphology-based filters are based on the set theory and use operator definition (opening, closing, dilation, and erosion). Mostly, they compare the heights of the neighboring points, working with acceptable elevation differences depending on the horizontal distances of the points. Filtering quality depends on the filter cell size; to improve filtering quality, morphological filters with gradually increasing cell size and threshold have been designed ([23–25]).

Segmentation-based filters divide the point cloud into segments, each segment is labeled as either terrain or object; success depends on the quality of the segmentation. They work with point height, intensity, height difference, or geometric attributes (area, perimeter) ([26–29]). Statistic-based filters are based on the fact that terrain points have a normal distribution in terms of height in a certain window, but an object or vegetation points violate this distribution. Based on this assumption, skewness and kurtosis parameters are calculated and used to judge whether a point is on the terrain or on an object ([30–31]). These are methods in which no threshold is specified, e.g., the method proposed by Bartels (skewness balancing, [30]) takes into account the skewness value of the surrounding point cloud and deletes the highest point from the cloud if the skewness is greater than 0. The remaining group of unclassified filters can include, for example, a hybrid filter [32], cloth-simulation filter [33], the multi-class classification filter using convolutional network [34, 35], or a combination of cloth simulation filter with progressive TIN densification [36]. Algorithms based on Deep Learning (neural networks) have also been investigated, e.g. [37–42], but these need to be trained on specific data and are therefore probably not yet widely used.

As none of these approaches is universally applicable, the evaluation of the suitability of individual filters for specific purposes has recently been the subject of many scientific papers [42–43] and so has their sensitivity analysis [44].

Most known filtering techniques have been developed primarily for point clouds derived from airborne laser scanning (ALS), the nature of which is significantly different from data acquired by systems mounted on small aerial vehicles (UAVs), mobile or static ground platforms (regardless of whether they were mounted with laser scanners or collect imagery for the photogrammetric derivation of the cloud). The latter types of scanning systems typically provide high coverage density and extremely detailed and dense point clouds. Such data have been in the past typically used predominantly for relatively flat areas covered with buildings or vegetation. At present, remote sensing is increasingly used for measurements of relatively small areas with rugged rocks, quarries, or similar objects where vegetation removal is highly complicated even for a human operator. Thus,

 doi:10.20944/preprints202208.0426.v1

special filters and algorithms that go beyond the "standard" techniques and are capable of utilizing the dense clouds provided e.g by UAV systems are being developed even for such specific situations [45–47].

Based on the above, it can be concluded that the general widely available ground filtering approaches are not suitable for many engineering applications, especially where rugged areas of smaller extent are concerned. Therefore, in this paper, we present a newly developed filtering algorithm designed particularly for dense point clouds – MVSR (Multi-View and Shift Rasterization). This algorithm allows acquisition of a terrain point cloud appropriately describing even the most rugged areas, which does not suffer from problems and artefacts typically found in geometric filters. In this algorithm, the terrain points are selected from the cloud individually as the lowest points of cells of a square grid, which is being gradually shifted in small steps and tilted about all three coordinate axes. In this paper, we aimed to: (i) present the principle of the novel filtering algorithm, (ii) test its performance on three areas differing in the degree of ruggedness and vegetation cover, and (iii) compare its performance to that of selected widely used filters.

2. Materials and Methods

The proposed algorithm differs from the commonly used ones mainly in that it assumes a massive number of redundant points – a situation common in e.g. in terrestrial, mobile, or UAV scanning, i.e., scanning with high detail. This assumption contrasts with the assumptions used in the majority of current algorithms (which were created for point clouds acquired by ALS). The algorithm does not aim to select all ground points existing in the point cloud but rather, it aims to identify a sufficient number of such points for accurate characterization of the course of the terrain with emphasis on the reliability of those points that were identified as terrain.

2.1. Algorithm description

The basic idea of the algorithm is that the lowest point from a certain area is likely to be a terrain point (or, to be more general, a point of the surface of interest covered by vegetation). Obviously, if such an area is square, this is similar to rasterization (but in rasterization, the lowest point detected in the cell is typically not left in its original location but used as a proxy for the whole square/cell and placed in its center). Without any doubt, the likelihood of the lowest point being a ground point increases with the increasing cell size. On the other hand, however, the larger the selected cell is, the fewer points are left to characterize the terrain. The basic premise for the choice of the cell size is that it must be larger than the largest object that may lie on the terrain (i.e., a hole in the terrain data caused, for example, by occlusion by vegetation under which there is no point on the terrain, a building, etc.). In the real world, such a cell must necessarily cover an area of at least several meters. Thus, if the point cloud is processed by its division into square cells of sufficient size (in the horizontal plane), the lowest point in each of these cells is very likely to represent terrain; the number of such points will, however, be very small, and many characteristic points of the terrain (e.g. the highest points of a ridge or pile) will be missing.

The presented method uses two techniques for point cloud densification and capturing the ground points even in the maxima (i.e., points with the highest ground elevation):

1. Moving the raster as a whole (i.e. shifting the cells in which the lowest point is identified) in steps much smaller than the cell size) in both horizontal axes (X, Y).;
2. Tilting (or, rather, rotation) of the raster around all 3 axes (X, Y, Z) changes the perspective for evaluation of the elevations of individual points in the given projection. After such tilting, the raster is again gradually shifted as in the previous

Preprints (www.preprints.org) | NOT PEER-REVIEWED | Posted: 25 August 2022 doi:10.20944/preprints202208.0426.v1

step, and points with the lowest elevation in each cell after each displacement are selected.

Fig. 1 shows the basic ideas of the algorithm – the idea of shifting and rotating the grid. The figure shows only a cross-section; note, however, that the algorithm itself works in 3D and, thus, if the cell size is large enough, the algorithm is able to bypass areas that are completely free of ground points (e.g., under a large tree; in such a case, the ground on the edge of the cell is selected and in the area without ground points, none are falsely selected).

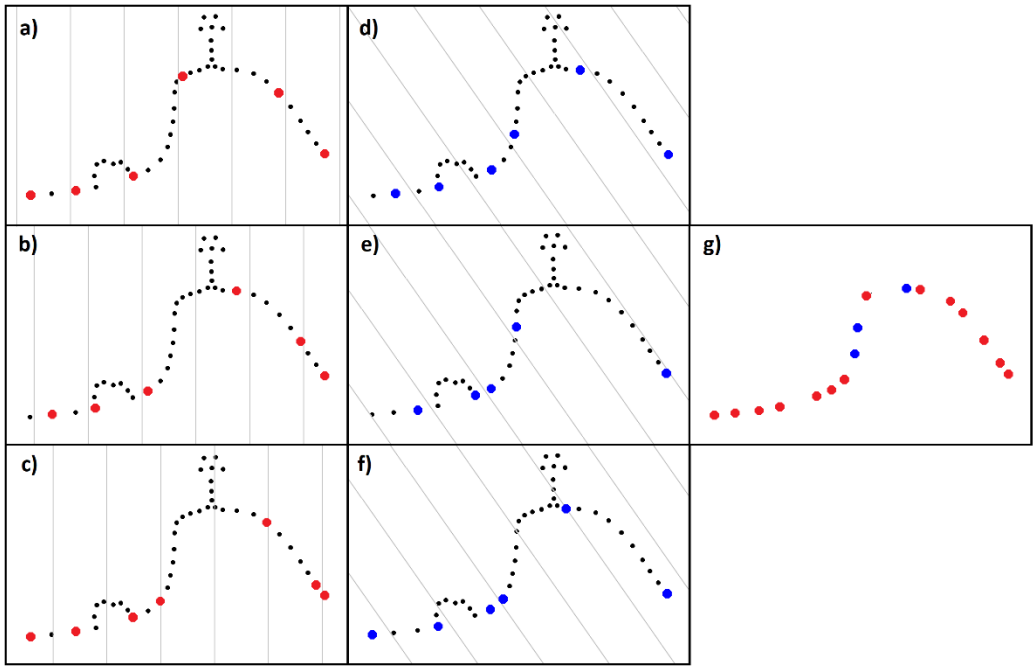

Figure 1. The principle of the method: a) – c) vertical raster in 3 steps (i.e., shifted 3 times) – red points; d) – f) rotated raster in 3 steps (i.e., one rotation shifted 3 times) – blue points; g) resulting terrain points identified in the respective color.

The algorithm in pseudocode is shown in Appendix A. The algorithm is designed to assign each point into a grid cell; if the assigned point is the lowest one in the cell at the time, it is recorded and the previous lowest point in the cell is deleted. In this way, all points are assigned and processed during a single pass for one position (shift and tilt) of the raster, which greatly reduces the computational demand compared to a situation in which all points within a cell would be first identified and the lowest of them subsequently selected. The algorithm is also suitable for easy parallelization; in our tests, 12 processors were used simultaneously.

The computational complexity, therefore, linearly increases with the number of cloud points), quadratically with the number of grid shifts, and of course, also increases with the increasing number of preset cloud rotations. The size of the grid (cell) determines the size of the objects that the method is able to bypass and, together with the grid shift size, also the detail of the resulting cloud.

It must be mentioned that if the edge of the cloud contains above-ground points, this thin margin will not be corrected automatically due to the oblique evaluation of the cloud and it must be removed during further processing (manually or simply by cropping the entire filtered point cloud, which is preferable).

2.2. Illustration of the algorithm performance

 doi:10.20944/preprints202208.0426.v1

The performance of the algorithm will be demonstrated on a simple example of data capturing a rugged and heavily forested hill. The point cloud covering an area of 16,700 m² was scanned by a UAV-lidar system UAV – DJI L1 (further information can be found in the Appendix B); after dilution to a 0.07 m minimum distance between points, it contains 2,995,078 points. The site can be described as a ridge on a flat area (Fig. 2) and, besides ruggedness, the data are characterized also by large holes in the terrain data caused by vegetation cover and a small stream running through the area (water absorbs the lidar beam).

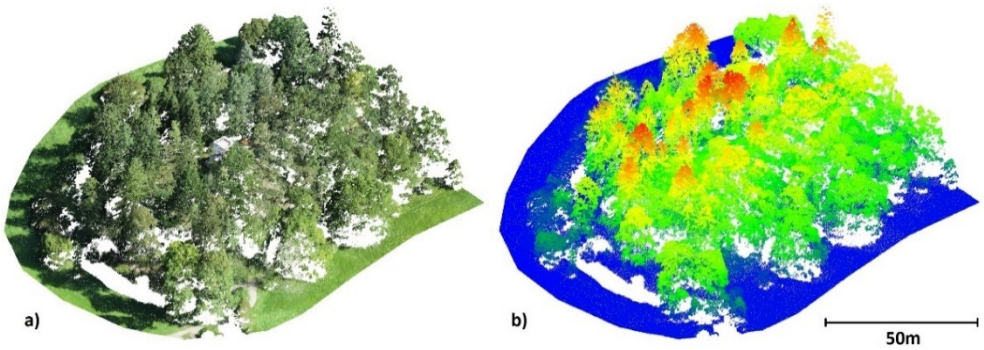

Figure 2. Illustration dataset: (a) true colors (b) elevation-coded data.

Fig. 3a) shows a ground point cloud resulting from the basic rasterization and calculation of the lowest point in each cell of a 10 x 10 m grid (without any shifts and tilts).

As the area size is approximately 140 m x 130 m, the number of ground points will be very small if using a 10 x 10 m cell. Given the cell size, these points are very likely to be indeed on the ground (and not on vegetation), but in terms of describing the landform, their density is certainly insufficient. Higher densities would be achievable by reducing the cell size, but in such a case, the cell would be likely in many cases smaller than the areas without ground data and filtering would be ineffective, identifying vegetation as ground points. Shifting the entire raster can lead to the potential identification of additional ground points. Figure 3(b) presents the situation after calculations using 5x5 displacements in the XxY direction (the grid was, therefore, shifted 5 times by 1/5 of the cell size in each direction). Here, we can observe the desired densification, but the terrain points on the vertices (or on the ridge as here) cannot be, on principle, correctly identified – in the vicinity of the ridge, any 10 x 10 m cell is bound to contain points with elevations lower than the ridge. This problem can be solved by changing the direction of the terrain view, i.e. by rotating the data (see Fig. 3 c, d, e - showing data filtered using individual rotations). Rotation also changes the projection of the cell on the terrain and, thus, changes the effective grid size, which also densifies the resulting cloud. Rotations should always be selected in a way corresponding to the estimated slopes of the surface (see below in the Methods) Fig. 3 f) shows the filtering result of the combined data from 18 rotations (a combination of -50 gon, 0 gon, and +50 gon for rotations about the X and Y axes; 0 and 50gon about the Z-axis), each of which was analyzed using 5x5 raster positions. Of the original approximately 3 million points, 29 thousand remain, with an average density of 1.5 points per m².

 doi:10.20944/preprints202208.0426.v1

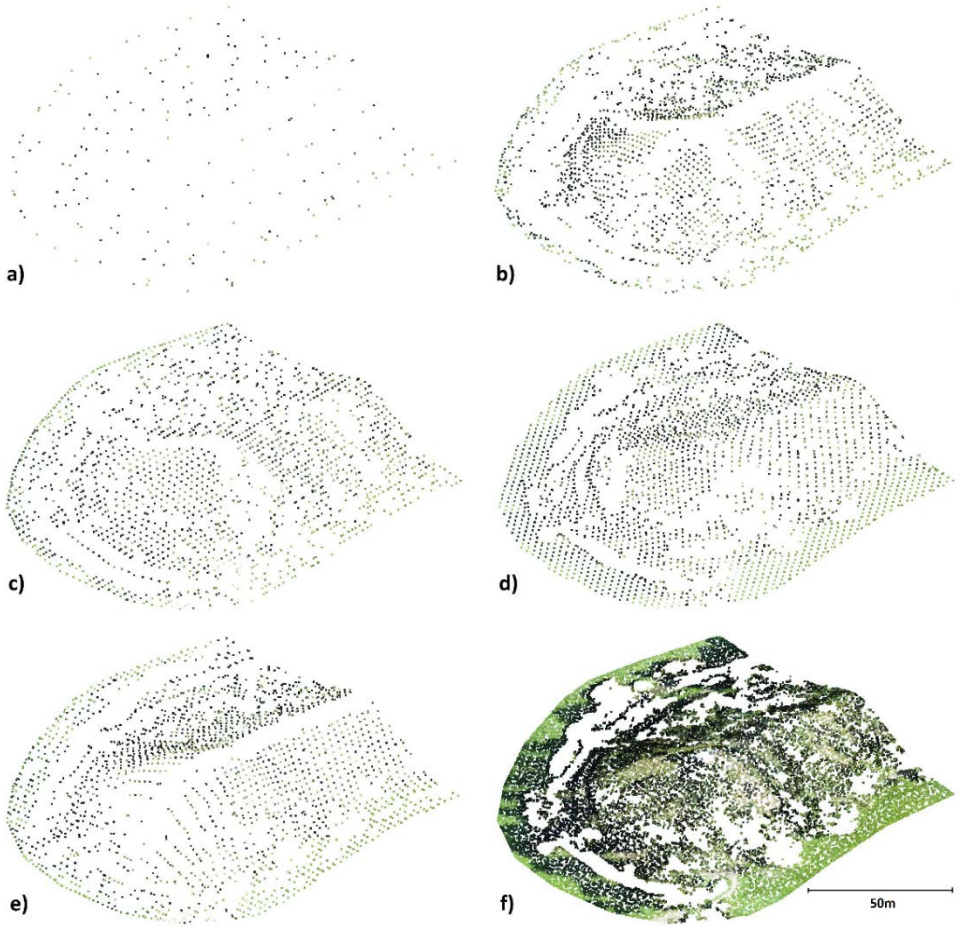

Figure 3. Illustration data – the gradual processing: a) vertical grid - only the first step b) vertical grid - 5x5 steps c) d) e) after one selected rotation - 5x5 steps f) the resulting ground point cloud constructed from all positional shifts and rotations.

Fig. 3 also demonstrates the presence of gaps in the data; this is most obvious along the ridge (e.g. b) and e)). This gap position changes with individual rotations according to the apparent positions of the ridge relative to the remaining points from the virtual bird's eye view. It is worth noting that the grid shift was also used as a part of the algorithm in [48], but without tilt (rotation) it is not possible to successfully filter areas close to horizontal and especially the tops (ridges) of landforms or overhangs. The result of filtering without using rotation can be seen in Fig. 3 b) with the already described gaps.

2.3. Data for testing

The algorithm has been tested on point clouds acquired by mobile and terrestrial scanning systems. We present results from terrains of varying complexity (different from the illustration dataset), from a virtually flat area through an extremely rugged and sloping rock face to a quarry area with a densely forested part of the surface, causing large gaps in terrain points. Lastly, as an example of an area with tall anthropomorphic objects, filtering of a rugged terrain with vegetation and bridge pillars is presented.

Site 1 (Fig. 4 a)) – a virtually flat terrain with low vegetation, area of 20,000 m^2, diluted to 1,408,072 points with a minimum distance between neighboring points of 0.07 m, acquired using a Leica Pegasus mobile scanner mounted on a car (further information can be found in the Appendix B). This dataset was selected as a basic one because it can be assumed that virtually any filter should be able to deal satisfactorily with its filtering.

Preprints (www.preprints.org) | NOT PEER-REVIEWED | Posted: 25 August 2022 doi:10.20944/preprints202208.0426.v1

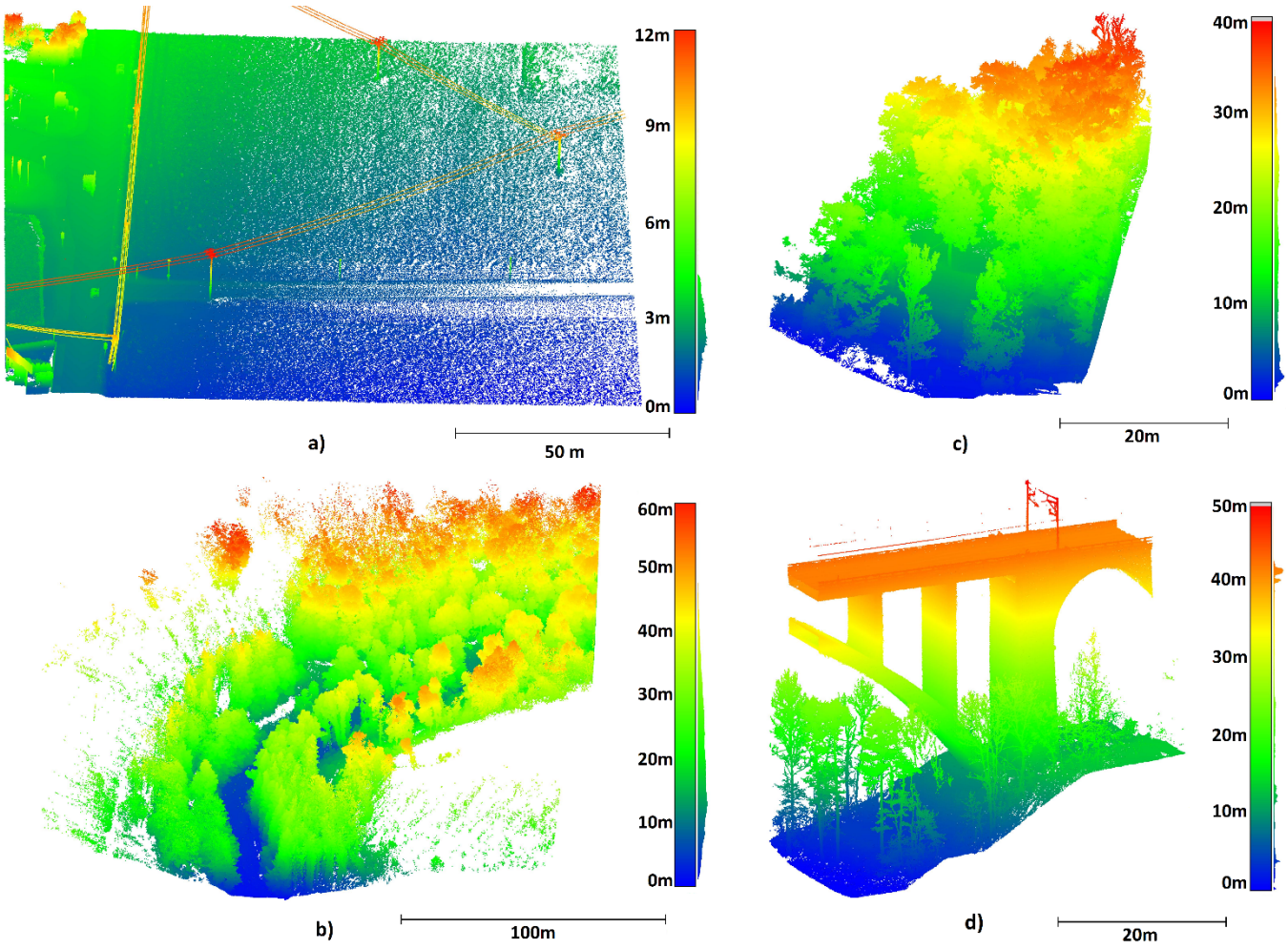

Figure 4. Testing point clouds colored by relative height a) Site 1 b) Site 2 c) Site 3 d) Site 4.

Site 2 (Fig. 4 b)) – rural road surrounded by forest on steep slopes, relatively rugged area of approx. 25,000 m², 10,016,451 points, diluted to 0.07 m, acquired with a Leica Pegasus mobile scanner mounted on a car (further information can be found in the Appendix B).

Site 3 (Fig. 4 c)) – a virtually vertical cliff covered with vegetation, nets, and structures, area of approx. 1240 m², diluted to 0.05 m resolution; 2,785,912 points in total, acquired with a Trimble X7 terrestrial scanner (further information can be found in the Appendix B). The data from this site contain high as well as medium and low dense vegetation.

Site 4 (Fig. 4 d)) – an area of approx. 1207 m² with rugged terrain, low and tall vegetation and tall bridge pillars combined with a curved bridge construction, diluted to a resolution of 0.07 m; 830,836 points in total; acquired by the combination of terrestrial 3D scanner Leica P40 (mainly the construction) and UAV photogrammetry using the DJI Phantom 4 RTK (more information can be found in the Appendix B).

2.4. Data processing and evaluation

The filter presented in this paper was programmed in the Scilab environment interpreted language (www.scilab.org, open-source software for numerical computation, version 6.1.1 was used). Since the latest versions of the environment do not allow parallel executions, the task was pre-divided into the required number of X parts (usually 12 on a 16-processor system) to speed up the computation.

 doi:10.20944/preprints202208.0426.v1

As the data differ in character, various settings were used (detailed in Table 1). Partial rotations about individual axes were used in all combinations. As mentioned above, the estimated slopes of the terrain serve as a basis for the selection of the rotation angles – the angles of rotation should (i) roughly correspond to and (ii) slightly exceed the angles between all normals of the surface and the vertical direction (see the high number of angles needed for Site 3 with extreme ruggedness). Note that if the steps are fine in one or two directions, the step in the remaining direction(s) can be somewhat greater as the combination of all rotations already ascertains sufficient detail.

Table 1. Parameters of MVSR filter settings for individual datasets.

Data	Raster size [m]	Number of shifts	Shift size [m]	Rotations		
				Alfa [gon]	Beta [gon]	Gamma [gon]
Site 1	1	10	0.1	-25; 0; 25	-25; 0; 25	-25; 0; 25
Site 2	5	10	0.5	-25; 0; 25	-25; 0; 25	0; 50
Site 3	1	10	0.1	0; 25; 50; 75; 90; 120	-50; 0; 50	-50; 0; 50
Site 4	7.5	25	0.3	-25; 0; 25	-25; 0; 25	-25; 0; 25

As the dataset for Site 3 is highly rugged and the surface is very steep, the range of rotations about the X-axis differs from those in other datasets. In Site 4, the gaps in ground data (represented by the base of the pillars) are notably bigger than in other sites; to overcome this, a greater raster size was chosen (7.5 m, i.e., bigger than the gaps) and a greater number of shifts (25 shifts) was used to achieve an appropriate detail.

The evaluation of the quality of MVRS ground filtering using standard methods is difficult in the used complicated datasets. In view of their density and ruggedness, the creation of a reference terrain model that would be used for determining Type I and Type II errors is practically impossible as no perfectly filtered data exist and even manual assessment would be highly dependent on individual judgment, thus associated with high uncertainty. Besides, the inherent dilution of the cloud would also bias such an evaluation. Another widely used approach using independent control points determined by GNSS or total station is not suitable here, either, as this approach is in this type of terrain burdened by the differences between methods (their accuracy, coverage, etc.).

As this study aimed to evaluate ground filtering quality, this can be only reliably performed using datasets created from the same original data.

For these reasons, the filtering quality was evaluated by comparison to the original cloud and to the results of filtering by widely used conventional filters. First, a visual comparison was performed and, subsequently, differences between the surface created from MVRS filtering results and those obtained by other filters (and with the lowest points from the original cloud) were calculated.

2.5 Filters selected for comparison

The evaluation of the quality of MVRS results was performed by comparing results to those obtained by selected conventional filters: Progressive Morphological Filter (PMF, [23]), Simple Morphological Filter (SMRF, [24]), Cloth Simulation Filter (CSF, [33]) and adaptive TIN models filter ([32], ATIN). PDAL software (http://pdal.io) was used for calculations using PMF and SMRF filters, CloudCompare v. 2.12 (www.cloudcompare.org) for CSF filter and lasground_new, a part of Lastools package (https://rapidlasso.com/lastools/), for ATIN.

Choosing optimal settings for those filters is quite complicated in the rugged areas (as shown, e.g., in [45]). For this reason, multiple settings were operator-tested to identify (for each site and filter) settings preserving the highest number of terrain points while removing the maximum amount of vegetation points. The selected settings for individual datasets and filters are shown in Table 2.

Preprints (www.preprints.org) | NOT PEER-REVIEWED | Posted: 25 August 2022 doi:10.20944/preprints202208.0426.v1

Table 2. Filtering parameters for individual filters and datasets (in metres or dimensionless).

Data	PMF	SMRF	CSF	ATIN
Site 1	cell size 1.0	cell 0.5	Cloth resolution 0.2 m	- wilderness
	initial distance 0.5	scalar 1	Classif. Threshold 0.1 m	- all_returns
	max distance 0.5	slope 3	Scene Slope	- offset 0.05
	max window size 1	threshold 0.1	Slope processing Yes	
	slope 1	window 1	Number of iterations 500	
Site 2	cell size 0.5	cell 0.4	Cloth resolution 0.1 m	- wilderness
	initial distance 1.0	scalar 0.2	Classif. Threshold 0.1 m	- all_returns
	max distance 1.0	slope 3	Scene Slope	- offset 0.05
	max window size 1.0	threshold 0.05	Slope processing Yes	
	slope 3	window 10	Number of iterations 500	
Site 3	cell size 0.3	cell 0.1	Cloth resolution 0.1 m	- wilderness
	initial distance 0.8	scalar 0.1	Classif. Threshold 0.3 m	- all_returns
	max distance 1.0	slope 3	Scene Slope	- offset 0.20
	max window size 0.5	threshold 0.1	Slope processing Yes	
	slope 3	window 1	Number of iterations 500	
Site 4	cell size 0.3	cell 0.4	Cloth resolution 0.1 m	- nature
	initial distance 0.5	scalar 0.3	Classif. Threshold 0.1 m	- all_returns
	max distance 1.0	slope 0.7	Scene Slope	- offset 0.10
	max window size 12	threshold 0.2	Slope processing No	
	slope 2	window 10	Number of iterations 500	

2.6 Visual evaluation

Visual evaluation of the results of MVRS and those of other filters was performed both on the level of entire surfaces and of profiles from selected potentially problematic areas.

2.7 Evaluation of the differences from the MVRS-based surface

This evaluation was performed as follows: MVSR-filtered data were used for the creation of TIN-approximating ground (MVSR-TIN surface), which was cropped at the edges to remove artifacts described above. Signed distance (+ above/ - below) of all points from the original cloud as well as from filtered clouds obtained by other filters was calculated and root mean square deviations of individual points left below/above the filtering result were calculated.

For the comparison with the original point cloud, only points below the MVSR-TIN surface are of importance (representing points that were omitted in the detection of the ground) while points above the MVSR-TIN surface obviously contain all vegetation.

Subsequently, the results of ground filtering by other filters were evaluated in the same way; in these, however, RMSD for points above the MVSR-TIN surface was also calculated to evaluate the quality of above-ground point removal. RMSD was calculated using the Equation 1:

$$\mathrm{RMSD} = \sqrt{\frac{\sum d^2}{n}}, \quad (1)$$

where d is the distance from the created surface approximation (TIN), and n is the number of points.

3. Results

The above-described filtering techniques were applied on the point clouds; Table 3 shows the number of cloud points before and after filtering using all algorithms.

 doi:10.20944/preprints202208.0426.v1

Table 3. The number of points in the original and filtered clouds.

Data	Original	PMF	SMRF	CSF	ATIN	MVSR
Site 1	1,408,072	1,244,526	1,126,268	1,128,881	959,390	1,028,481
Site 2	10,016,451	2,009,885	1,407,364	1,251,470	701,946	280,087
Site 3	2,785,912	592,083	439,181	502,067	420,902	316,611
Site 4	830,836	190,795	173,228	153,196	166,794	66,791

3.1 Visual evaluation

The first region is practically flat; in principle, any filter should work satisfactorily here. All filters yielded similar results; for this reason, only the result of the MVSR filter is shown (Fig. 5).

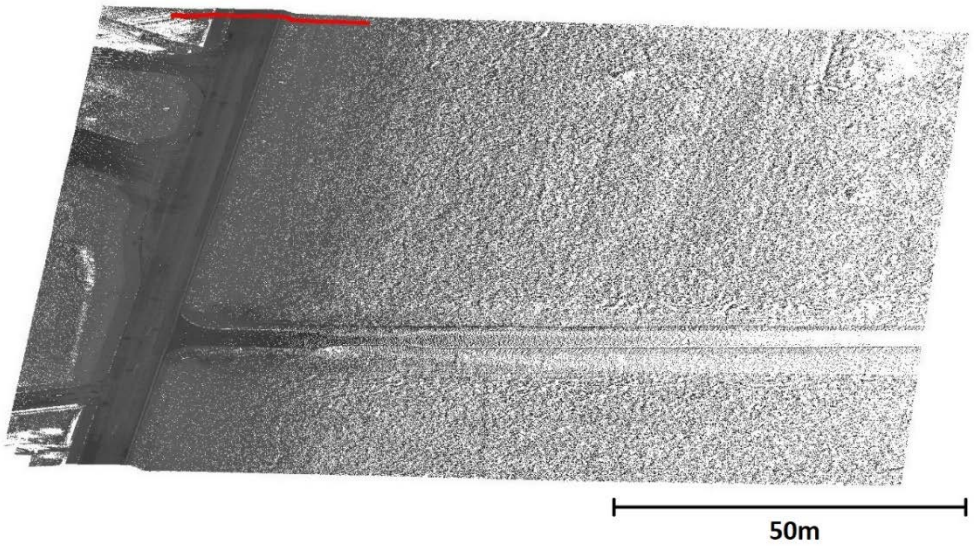

Figure 5. Site 1: Data after MVSR filtering, red line indicates the locations of profiles presented in Fig. 6.

Since the quality of ground filtering cannot be distinguished when displaying the entire cloud in a single image, it will be presented on selected profiles showing both the original data and the data obtained by the filters under comparison (including the MVSR filter). The profile shown in Fig. 6 shows the success of both the geometrical filters and MVSR filters in basic filtering. It is worth noting that in parts of the profile with low vegetation (most likely grass), the MVSR profile is significantly smoother (the profile curve aggregates points from a 0.5 m wide strip of the point cloud and, hence, it cannot be perfectly thin and smooth).

Clearly, ATIN and MVSR have the best and very similar results, with MVSR results being slightly more complete. Filtering results of all filters are in the Appendix C.

 doi:10.20944/preprints202208.0426.v1

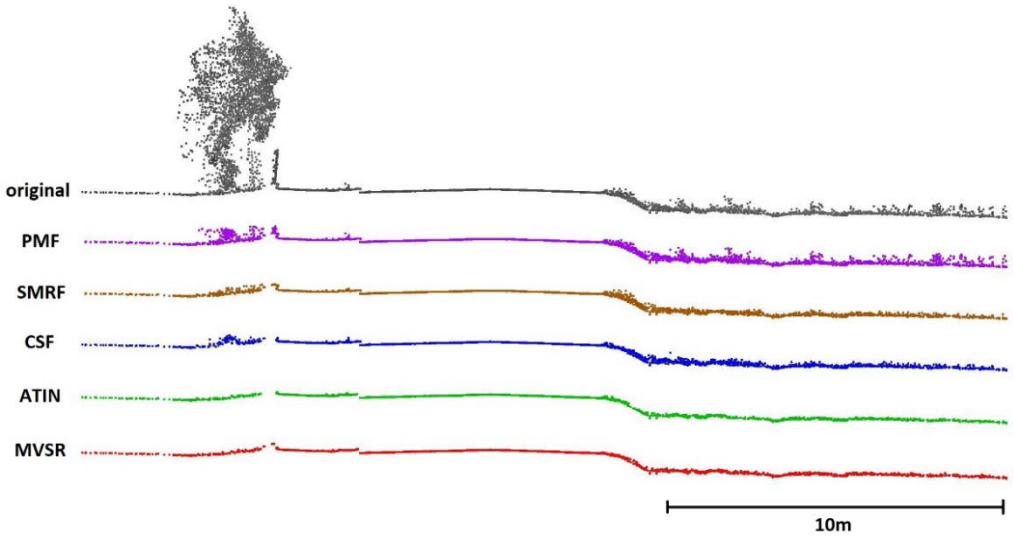

Figure 6. Site 1 - Profile; grey – the original cloud; purple - PMF; brown – SMRF; blue – CSF; green – ATIN; red – MVSR.

The second area captured by Data 2 is significantly more rugged, covered with dense, both tall and low, vegetation. Ground filtering in this area is no longer a simple matter, the slopes are quite steep and the point density decreases rapidly with the distance from the vehicle path. The ground surface data are greatly affected by tree cover. An overall view of the CSF and MVSR filtering results is shown in Fig. 7. Results of all filters are in the Appendix C.

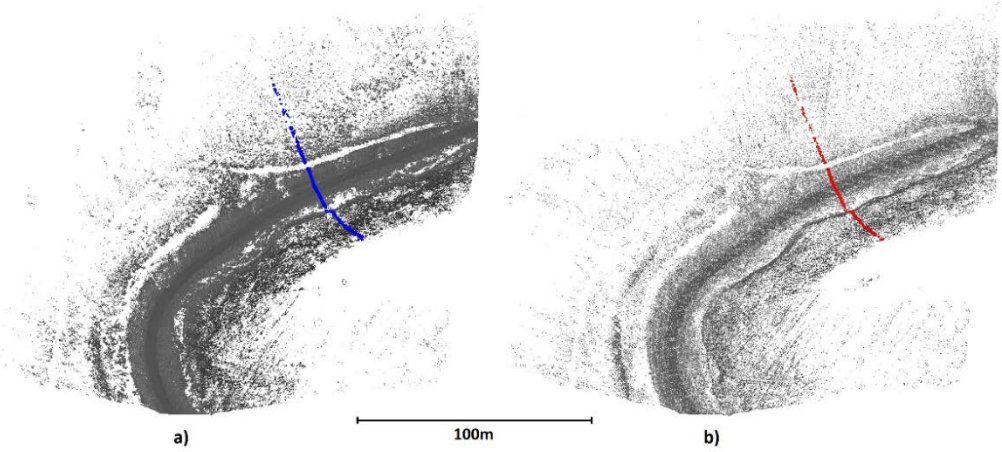

Figure 7. Site 2 after a) CDF and b) MVSR filtering; the profiles detailed in Fig. 8 are indicated by the blue (CSF) and red (MVSR) lines.

After comparing the results, we can conclude practically the same as in the previous case (Fig. 8). MVSR appears to correctly select ground points even in the areas with very sparse data (left and right edges of the image), with ATIN performing second best.

Preprints (www.preprints.org) | NOT PEER-REVIEWED | Posted: 25 August 2022 doi:10.20944/preprints202208.0426.v1

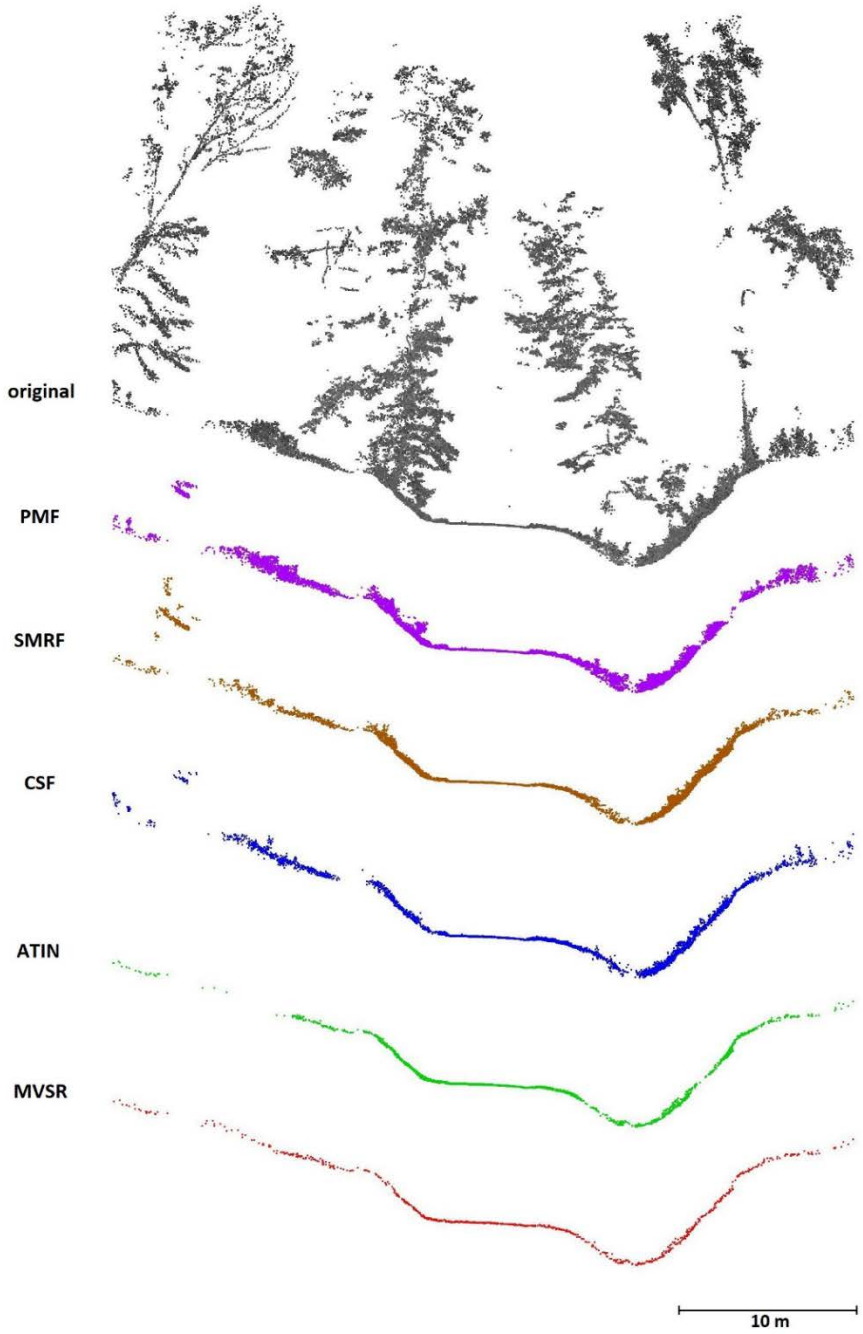

Figure 8. Profiles from Site 2 filtering: grey – the original cloud; purple - PMF; brown – SMRF; blue – CSF; green – ATIN; red – MVSR.

The numbers of points of individual filtered point clouds differ greatly (Table 2). While the original cloud consists of 10 mil. points and the CSF point cloud of 1.25 mil points, MVSR identified only 0.28 mil. ground points. However, as obvious from the figures, even this is sufficient for terrain description. On the road (center) the point density is approx. 45 points/m^2, on the adjacent slopes (outside covered-up areas), there are about 30 points/m^2.

It can be, therefore, concluded that the MVSR algorithm in this case successfully filtered the ground and, in addition, suitably and appropriately diluted the point cloud. Such an approx. 1:5 reduction in the number of points in the cloud will also bring a significant benefit for the simplification of further processing.

 doi:10.20944/preprints202208.0426.v1

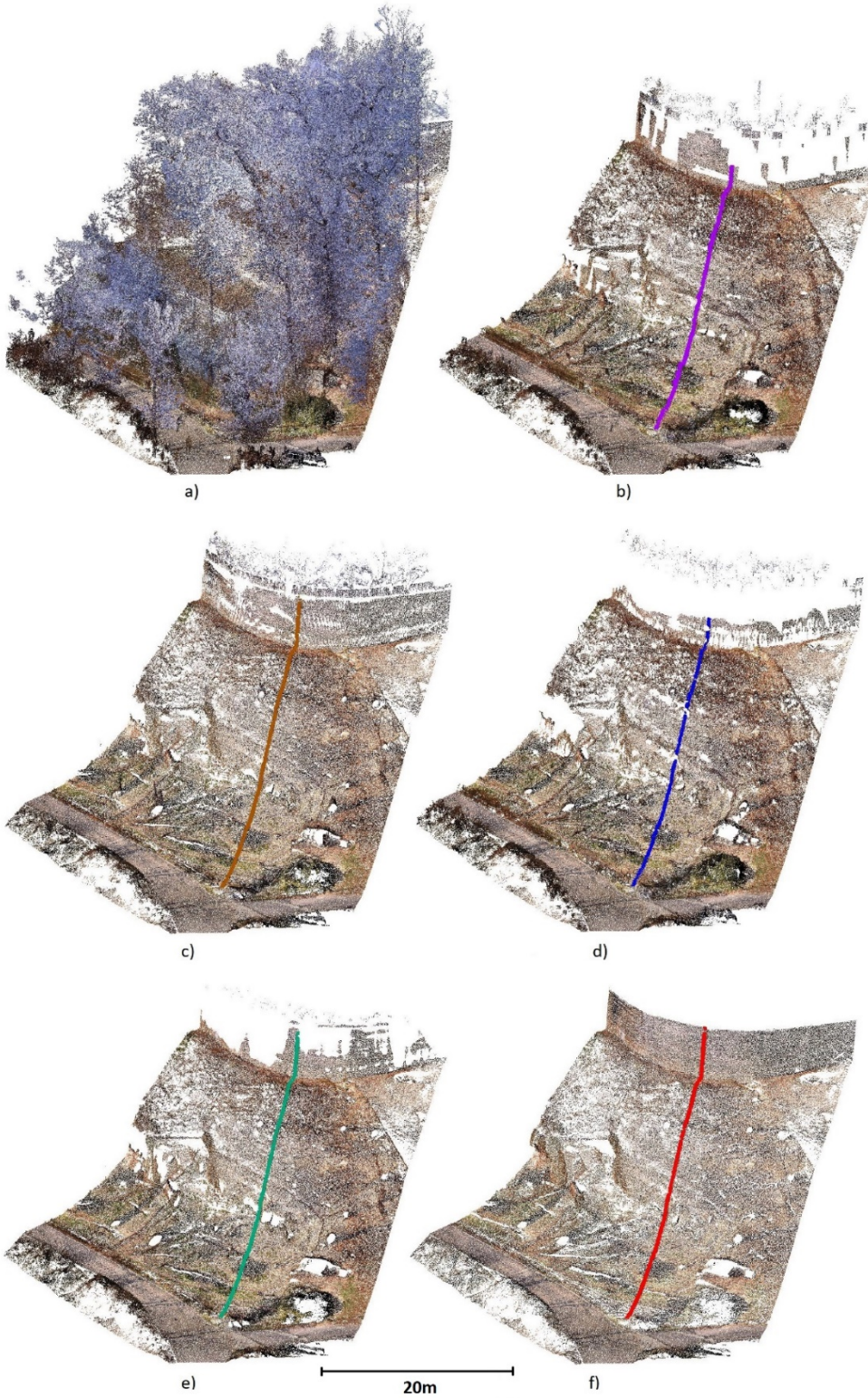

Figure 9. Site 3 a) original b) after PMF filtering, c) after SMRF filtering, d) after CSF filtering, e) after ATIN filtering, f) after MVSR filtering.

The area where Data 3 was acquired is a rugged steep cliff, practically vertical in the upper part; it is, therefore, of high complexity and highly problematic for both capture and subsequent evaluation. In such an area, the filtering results differ a lot. For this site, results from all filters are shown as in this area, the differences in the filtering success are

Preprints (www.preprints.org) | NOT PEER-REVIEWED | Posted: 25 August 2022 doi:10.20944/preprints202208.0426.v1

best visible. The data processed by CSF are visibly full of holes, especially where the terrain slope is higher or under an overhang (center of the left part in the figure).

To capture the ruggedness, shape, and steepness of the area, the grid tilting (explained in methods) used multiple angles, even as high as 120 deg, which allowed us to capture even the area under the overhang (Fig. 9 f).

The profiles show similar results as for previous sites but in this case, the differences are even greater (Fig. 10).

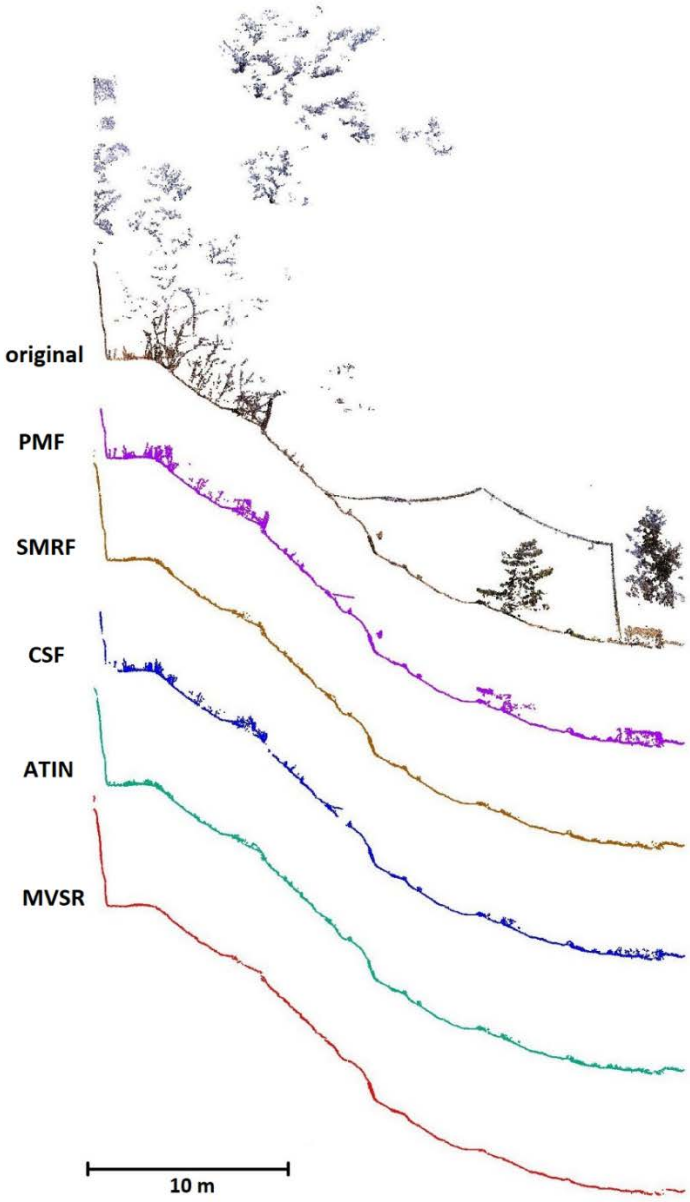

Figure 10. Profiles from Site 3 filtering grey – the original cloud; purple - PMF; brown – SMRF; blue – CSF; green – ATIN; red – MVSR.

In Site 4, the surface is somewhat less rugged than in Site 3; however, the tall bridge pillars and supports, the contact of which with the terrain is not just perpendicular, represents the dominant filtering problem in this area. The results of CSF and MVSR filtering are shown in Fig 11a and 11b, respectively. Results of remaining filters are similar to CSF and are presented in the Appendix C (Fig. C4).

Preprints (www.preprints.org) | NOT PEER-REVIEWED | Posted: 25 August 2022 doi:10.20944/preprints202208.0426.v1

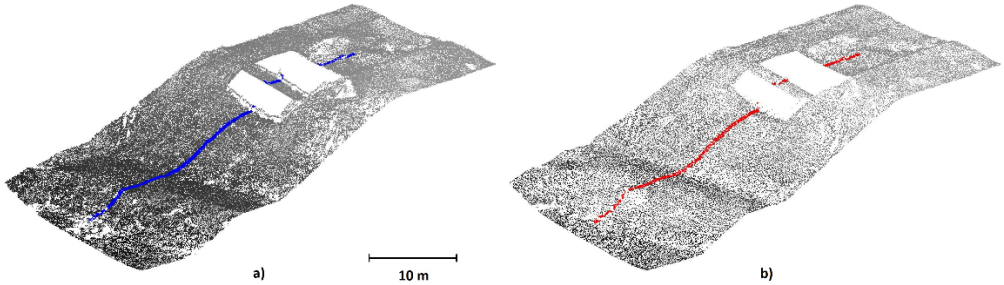

Figure 11. Site 4 a) after CSF filtering, b) after MVSR filtering

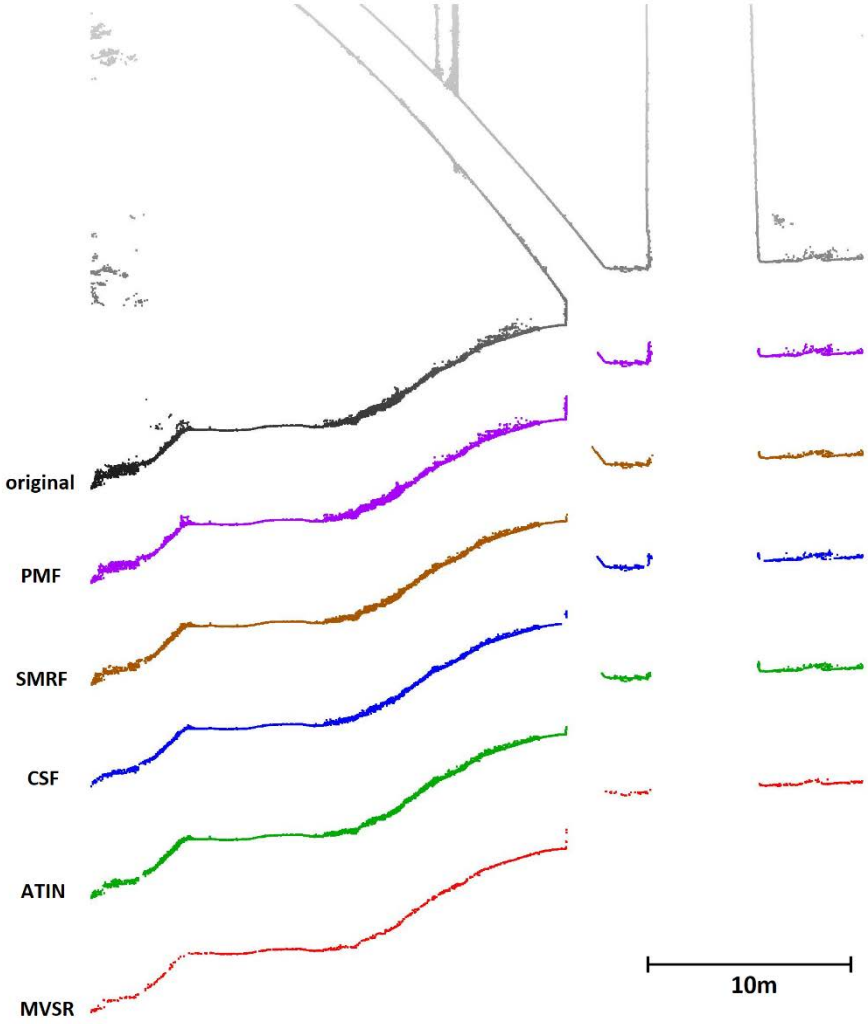

Figure 12. Profiles from Site 4 filtering (the upper part of the cloud describing the bridge, which plays no role in this evaluation, is cropped): grey – the original cloud; purple - PMF; brown – SMRF; blue – CSF; green – ATIN; red – MVSR.

Profiles in Fig. 12 show that even in this anthropomorphic site, the MVRS filter offers the smoothest and thinnest profile of all tested algorithms. Note that in places where the pillars are in contact with the ground, all filters identify a part of the pillar surfaces as ground. Again, the MVRS filter performed best of all used filters (i.e., identifying the smallest area of the pillar surfaces as ground – only on a single pillar surface).

3.2 Comparison of point clouds with an MVSR-based surface

 doi:10.20944/preprints202208.0426.v1

The overall RMSDs of points of the original point cloud found below the MVSR-generated surface in individual study sites are 0.7 cm, 2.5 cm, 0.6 cm and 1.7 cm for Sites 1, 2, 3 and 4, respectively. This indicates that the MVSR filter indeed selected the lowest points in the cloud. This is comparable with the results of the remaining tested filters, all of which had similar RMSDs of points below the MVSR-generated cloud (Tab. 4). In other words, all filters were capable of very good detection of the lowest points.

However, RMSDs of the filtering results obtained through other filters (taking into account only points found above the MVSR-generated surface) ranged from 4.5 cm to 95 cm, indicating a much thicker layer of ground filtered points and a higher amount of above-ground points left in the clouds after filtering). On the flat surface (Site 1), all filters yielded satisfactory results while at Sites 2 and 3, only the ATIN filter performed similarly well as the MVSR filter.

In Site 4, the situation is different due to the large gaps in ground data caused by the pillars – the bigger pillar is 10 m wide and about 5.5 m long at the point of contact with the ground. To perform successfully, the filters including MVSR need different settings than in the previous scenarios. This particularly affected the ATIN filter; where the "wilderness" setting that was successfully used in the previous sites (with a default step of 3 m) provided better vegetation filtering but above the gaps, parts of unfiltered pillars (up to the height of 14 m) were filtered as ground. For this reason, the setting had to be changed to "nature" (default step size of 5 m).

The RMSD above the MVSR surface for the original cloud shows basically just the average vegetation height.

Results of the ATIN filter implemented in the lasground_new software are the most comparable to those obtained by MVSR filtering; this also corresponds to the profiles shown in the previous chapter.

Table 4. RMSDs of the original cloud and data from individual sites ground-filtered using various filters compared to MVSR – based surface.

Data	Original [m]		PMF [m]		SMRF [m]		CSF [m]		ATIN [m]	
	Above	Below	Above	Below	Above	Below	Above	Below	Above	Below
Site 1	2.434	0.007	0.072	0.015	0.043	0.014	0.099	0.007	0.048	0.060
Site 2	10.339	0.025	0.631	0.026	0.950	0.028	0.395	0.025	0.045	0.027
Site 3	7.764	0.006	0.270	0.003	0.211	0.003	0.316	0.006	0.074	0.002
Site 4	20.238	0.017	0.145	0.010	0.098	0.010	0.099	0.017	0.080	0.017

4. Discussion

Many papers aiming at testing filters and selecting those best suited to the particular purpose have been published. For example, Moudry et al. [42] tested ground filtering of low-density ALS data capturing a slopy terrain of a spoil heap employing largely the same filters as this paper and comparing filtering results to control points measured using total station. Similar to our study, ATIN also performed very well in their work (root mean square error, RMSE, 0.15 m), followed by SMRF (0.17 m), PMF (0.18 m), and CSF (0.19 m); nevertheless, the differences between results of individual filters were relatively small. Štular et al. [49] tested a variety of filters for the determination of ground from low-density ALS data for archeological purposes. The terrain analyzed in their study was much more rugged with many projections. Again, ATIN was among the best performing filters. However, data on ground filtering of point clouds of a density as high as in our paper capturing rugged areas are practically non-existent in the literature.

The presented MVSR algorithm works on an entirely different principle not only compared to "classical" geometric filters that create an approximation of the surface using the selected points and then use a threshold to select the terrain points but even to other alternative approaches such as that presented previously by our group [45]. Unlike all of these, this algorithm selects the lowest points from the cloud even if only few such points

 doi:10.20944/preprints202208.0426.v1

are present and, as a result of this scarcity of ground points, they fail to form an algorithmically discernible surface necessary for filtering using the above-mentioned approaches.

The main features of our algorithm, therefore, are:

1. No approximations, simplifications, assumptions of the terrain are made;
2. The filtering step also dilutes the point cloud;
3. Compared with the common geometric filters, this one can be used for much more complex terrains, and, therefore, is much more versatile;
4. The computational demands increase approx. quadratically with increasing required detail (due to the number of raster shifts and raster size);
5. Like all filtering methods, this one also needs verification by an operator; here, typically, a thin layer of filtering artifacts on the edges of the area needs to be removed either manually or simply by cropping by (typically) several decimeters to a few meters;
6. Where a dense point cloud is needed, the MVSR method could be also used as the first step of an advanced multistep algorithm for the acquisition of the first terrain approximation, after which the remaining points can be identified based on a threshold as in standard filters.

Although this algorithm could work for ALS scanning data, it is primarily designed to work with high-density data of a local character with a high surface density in complex terrain measured at a short distance (UAV lidar, mobile lidar, terrestrial 3D scanner, SfM method). We should, however, mention a potential pitfall of this algorithm – outliers below the real terrain that the algorithm would detect as terrain points. This is not much of a problem for lidar data used in our paper as during the initial lidar data processing, such outliers are typically removed by the manufacturer-provided software but this problem might occur when working with SfM data. In such a case, the outliers should be removed by pre-filtering using, e.g., noise removal filters.

The algorithm is primarily designed for dense point clouds of nature-close environments (as urban landscapes, typically formed by buildings and planar areas, do not typically need particularly strong vegetation removal algorithms). However, as illustrated in Site 4, which is highly anthropomorphic, the algorithm can work well even in such areas providing that the cell size is set to be larger than the largest gap in the ground points. This, however, has to be compensated by the use of a greater number of stepwise shifts to achieve the terrain model of sufficiently fine detail.

Due to the high computational complexity with a large number of shifts of the base raster, the data can be with advantage reduced gradually. In other words, a smaller window and a smaller number of shifts could be used in the first pass, thus reducing the total number of points (especially above-ground points), and subsequently, a second pass with a larger window and a larger number of shifts could be employed on thus diluted data. Such specific combinations of parameters for stepwise reduction are currently investigated and will be the subject of future papers.

5. Conclusions

The novel MVSR ground filtering method presented in this paper was proven to be highly effective. Its testing on four point clouds obtained using various methods at sites with varying ruggedness and vegetation cover and comparison of the performance with other widely used filters (ATIN -Lastools, PMF - PDAL, SMRF - PDAL, CSF - CloudCompare) showed it to be superior to those filters (especially in the terrain with the greatest ruggedness and vegetation cover), with ATIN performing the best of the rest. This was shown both on the visual presentation of the filtered point clouds and by evaluation of the distance of the MVRS-based surface from the original point cloud and from the ground data acquired using the other filters.

 doi:10.20944/preprints202208.0426.v1

The selection of the lowest points in various positions and angles leads, besides the identification of the lowest points in the cloud, also to a dilution of the point cloud. Thus, we can assume that the presented filter can be also used in combined approaches with this filter acting as the first step for creating an approximation of the terrain that can be subsequently densified by the standard threshold-based approach employed in other filters.

Author Contributions: Conceptualization, M.Š.; methodology, M.Š.; software, M.Š.; validation, R.U. and L.L.; formal analysis, M.Š. and R.U.; investigation, L.L.; writing—original draft preparation, M.Š.; writing—review and editing, R.U. and L.L.; visualization, M.Š.; funding acquisition, R.U. All authors have read and agreed to the published version of the manuscript.

Funding: This research was funded by the Grant Agency of CTU in Prague—grant number SGS22/046/OHK1/1T/11 „Optimization of acquisition and processing of 3D data for purpose of engineering surveying, geodesy in underground spaces and 3D scanning“ and by Technology Agency of the Czech Republic – grant number CK03000168 „Intelligent methods of digital data acquisition and analysis for bridge inspections“.

Conflicts of Interest: The authors declare no conflict of interest. The funders had no role in the design of the study; in the collection, analyses, or interpretation of data; in the writing of the manuscript; or in the decision to publish the results.

Appendix A: MVSR algorithm code

Below, the algorithm pseudocode is shown. The structure of the data is very simple – it is a matrix where details of every point are in a single line, with the first three numbers always representing the point coordinates (X, Y, Z); additional point properties (such as RGB color components, intensity, etc.) are preserved but not used during filtering.

```
Points =  [ (1) x1 y1 z1 R G B ...
            (2) x2 y2 z2 R G B ...
             .
             .
            (p) xp yp zp R G B ...]
```

First, have a look at the constants and basic functions used in the algorithm:

0. Calculation parameters

Raster cell size:

```
RasterSize = R
```

Number of shifts:

```
NumberofShifts = N
```

Shift size

```
Shift = R/N
```

1. Reduction of the coordinates of the entire point cloud in a way ensuring that the minimum X, Y, and Z coordinates are equal to zero.

```
function Result = ReduceCoords(Points)
 Xm = min(Points(:,1));
 Ym = min(Points(:,2));
 Zm = min(Points(:,3));

  For i = 1:p
    Result(i, :) = Points(i,:) – [Xm Ym Zm]
  end;
End;
```

2. Rotation of the entire point cloud by defined angles about individual axes

Preprints (www.preprints.org) | NOT PEER-REVIEWED | Posted: 25 August 2022 doi:10.20944/preprints202208.0426.v1


```
function Result = RotatePoints(alfa, beta, gama, Points)
 RotX = [1      0         0;
        0  cos(alfa)  sin(alfa);
        0 -sin(alfa)  cos(alfa)]
 RotY = [cos(beta)  0   -sin(beta);
            0      1       0;
        sin(beta)  0    cos(beta)]
 RotZ = [cos(gama)  sin(gama)   0;
        -sin(gama) cos(gama)   0;
           0          0        1]
 Rot = RotZ*RotX*RotY;

 For i = 1:p
    Result(i, :) = (Rot*Points(i,:)')'
 end;
End;
```

3. Shift of the X and Y coordinates by a predefined value

```
function Result = ShiftPoints(Sx, Sy, Points)
  For i = 1:p
    Result(i,:) = Points(i,:) + [Sx Sy 0]
  end;
End;
```

4. Search for the point with the lowest elevation in each raster cell

```
function rastr = Rasterize(RasterSize, Points)
 max_x = max(Points(:,1));
 max_y = max(Points(:,2));

 limit_x = ceil(max_x/ RasterSize);
 limit_y = ceil(max_y/ RasterSize);
 rastr = zeros((limit_x, limit_y);

 for i = 1:p do
    x = floor(Points(i,1)/RasterSize)+1;
    y = floor(Points(i,2)/RasterSize)+1;
    if rastr(x,y) == 0 then
        rastr(x,y) = i
       else
           if Points(i,3) < Points(rastr(x,y),3) then
               rastr(x,y) = i;
           end;
       end;
 end;
End;
```

5. Saving the identified data – this is solely a routine programming issue of data management.

```
function result = SaveLowestPoints(LPointsID, Points)

//here, the storage pathways and form are to be programmed.
End;
```

6. The program itself

```
PointsC = ReduceCoords(Points)
For alfa = [alfa1, alfa2, …, alfam]
 For beta = [beta1, beta2, …, betan]
  For gama = [gama1, gama2, …, gamao]
```

 doi:10.20944/preprints202208.0426.v1


```
        PointsR = RotatePoints(alfa, beta, gama, PointsC)
        PointsR = ReduceCoords(PointsR)
        For SX = 0:N
           For SY = 0:N
              PointsS = ShiftPoints(SX*Shift, SY*Shift)
              LowestPointsID = RasterizePoints(PointsS)
              SaveLowestPoints(LowestPointsID, Points)
           end;
        end;
     end;
    end;
  end;
```

Appendix B: Scanning systems used for data acquisition

DJI Zenmuse L1 UAV scanner

For the acquisition of the illustration dataset the UAV scanner DJI Zenmuse L1 was used, it was mounted on the DJI Matrice 300 quadrocopter, the basic characteristics of both devices are given below in Table B1 and B2. Further information can be found on the manufacturer's website (https://www.dji.com).

Table B1. Basic characteristics of the DJI Zenmuse L1 laser scanner.

Dimensions	152 × 110 × 169 mm
Weight	930 ± 10 g
Maximum measurement distance	450 m at 80% reflectivity,
Recording speed	190 m at 10% reflectivity
System accuracy (1σ)	Single return: max. 240 000 points/s;
Distance measurement accuracy (1σ)	Multiple return: max. 480 000 points/s
Beam Divergence	Horizontal: 10 cm per 50 m;
Maximum registered reflections	Vertical: 5 cm per 50 m
RGB camera sensor size	3 cm per 100 m
RGB camera effective pixels	0.28° (Vertical) × 0.03° (Horizontal)

Table B2. Basic characteristics of the UAV DJI Matrice 300.

Weight	Approx. 6.3 kg (With One Gimbal)
Max. transmitting distance (Europe)	8 km
Max. flight time	55 min
Dimensions	810 × 670 × 430 mm
Max. payload	2.7 kg
Max. speed	82 km/h

 doi:10.20944/preprints202208.0426.v1

Leica Pegasus mobile scanner

For the acquisition of the point cloud on Site 1 and 2 the mobile system Leica Pegasus Two was used, the basic characteristics the device are given below in Table B3. Further information can be found on the manufacturer's website (https://leica-geosystems.com/).

Table B3. Basic characteristics of the Leica Pegasus Two scanner.

Weight	51 kg
Dimensions	60 x 76 x 68 cm
Typical horizontal accuracy (RMS)	0.020 m
Typical horizontal accuracy (RMS)	0.015 m
Laser scanner	ZF 9012
Scanner frequency	1 mil points per second
Other accessories and features	Cameras
	IMU
	Wheel sensor
	GNSS – GPS and GLONASS

Trimble X7 terrestrial scanner

For the acquisition of the point cloud on Site 3 the 3D terrestrial scanner Trimble X7 was used, the basic characteristics the device are given below in Table B4. Further information can be found on the manufacturer's website (https://geospatial.trimble.com).

Table B4. Basic characteristics of the Trimble X7 3D scanner.

Weight	5.8 kg
Dimensions	178 mm x 353 mm x 170 mm
Laser wavelength	1550 nm
Field of view	360° x 282°
Scan speed	Up to 500 kHz
Range measurement principle	Time-of-flight
Range noise	< 2.5 mm / 30 m
Range accuracy (1 sigma)	2 mm
Angular accuracy (1 sigma)	21″
Other important features	Sensors' autocalibration
	3 coaxial calibrated 10 MPix cameras
	Automatic level compensation (in range ±10°)
	Inertial navigation system for auto-registration

 doi:10.20944/preprints202208.0426.v1

Leica P40 terrestrial scanner

For the acquisition of the point cloud on Site 4 the 3D terrestrial scanner Leica P40 was used, the basic characteristics the device are given below in Table B5. Further information can be found on the manufacturer's website (https://leica-geosystems.com).

Table B5. Basic characteristics of the Leica P40 scanner.

Weight	12.25 kg
Dimensions	238mm × 358mm × 395mm
Laser wavelength	1550 nm / 658 nm
Field of view	360° x 290°
Scan speed	Up to 1 mil point/ s
Range measurement principle	Time-of-flight
Range accuracy (1 sigma)	1.2 mm + 10 ppm
Angular accuracy (1 sigma)	8″
Other important features	Dual-axis compensator (accuracy 1.5″) Internal camera 4 MP per each 17°×17°, colour image; 700 MP for panoramic image

DJI Phantom 4 RTK

For the acquisition of the point cloud on Site 4 the also the DJI Phantom 4 RTK UAV was used, the basic characteristics the device are given below in Table B6. Further information can be found on the manufacturer's website (https://dji.com).

Table B6. Basic characteristics of the DJI Phantom 4 RTK UAV.

Weight	1.391 g
Max. transmitting distance (Europe)	5 km
Max. flight time	30 min
Dimensions	250 × 250 × 200 mm (approx.)
Max. speed	58 km/h
Camera resolution	4864 x 3648

 doi:10.20944/preprints202208.0426.v1

Appendix C: Filtering results for all sites and filters

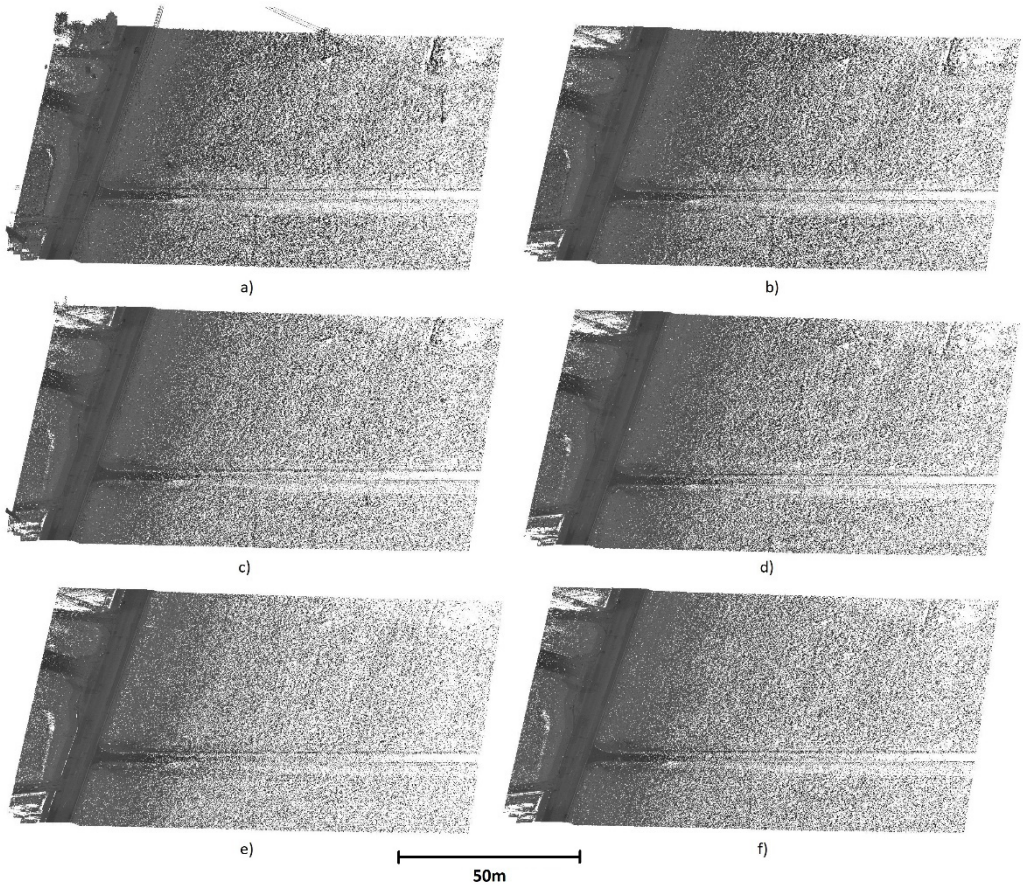

Figure C1. Results of filtering of Site 1 a) original data b) after PMF filtering, c) after SMRF filtering, d) after CSF filtering, e) after ATIN filtering, f) after MVSR filtering.

 doi:10.20944/preprints202208.0426.v1

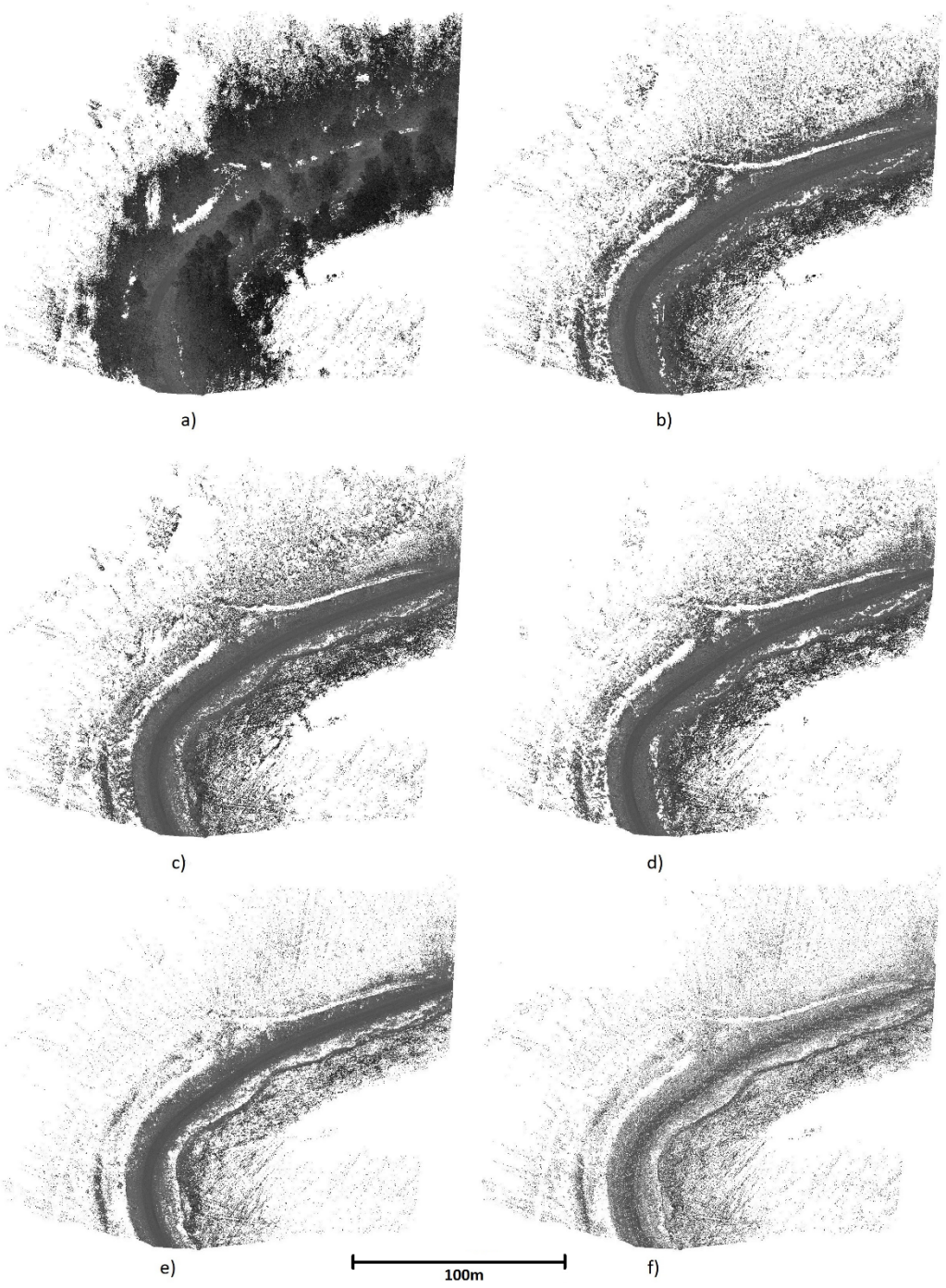

Figure C2. Results of filtering of Site 2 a) original data b) after PMF filtering, c) after SMRF filtering, d) after CSF filtering, e) after ATIN filtering, f) after MVSR filtering.

Preprints (www.preprints.org) | NOT PEER-REVIEWED | Posted: 25 August 2022 doi:10.20944/preprints202208.0426.v1

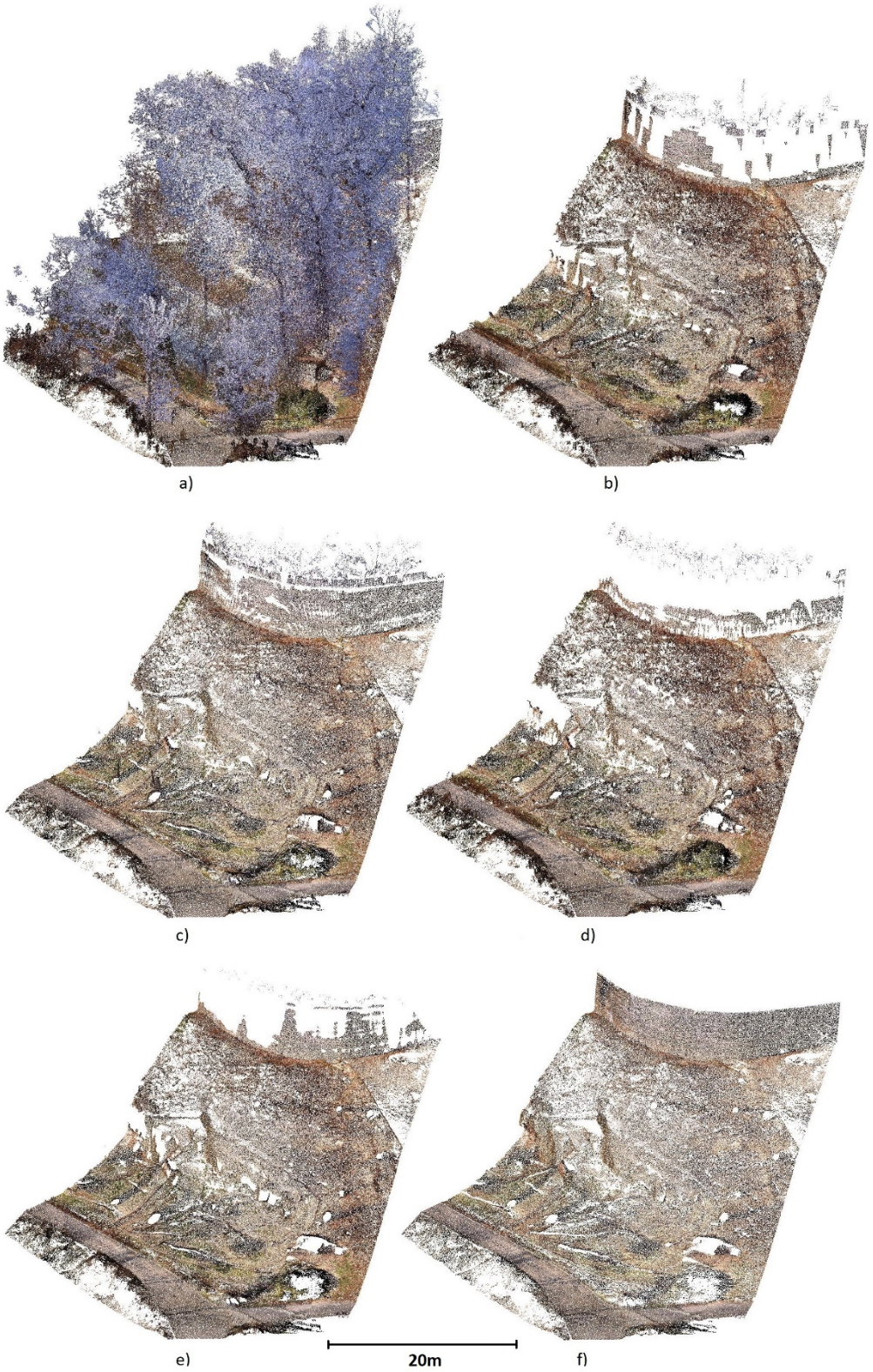

Figure C3. Results of filtering of Site 1 a) original data b) after PMF filtering, c) after SMRF filtering, d) after CSF filtering, e) after ATIN filtering, f) after MVSR filtering.

 doi:10.20944/preprints202208.0426.v1

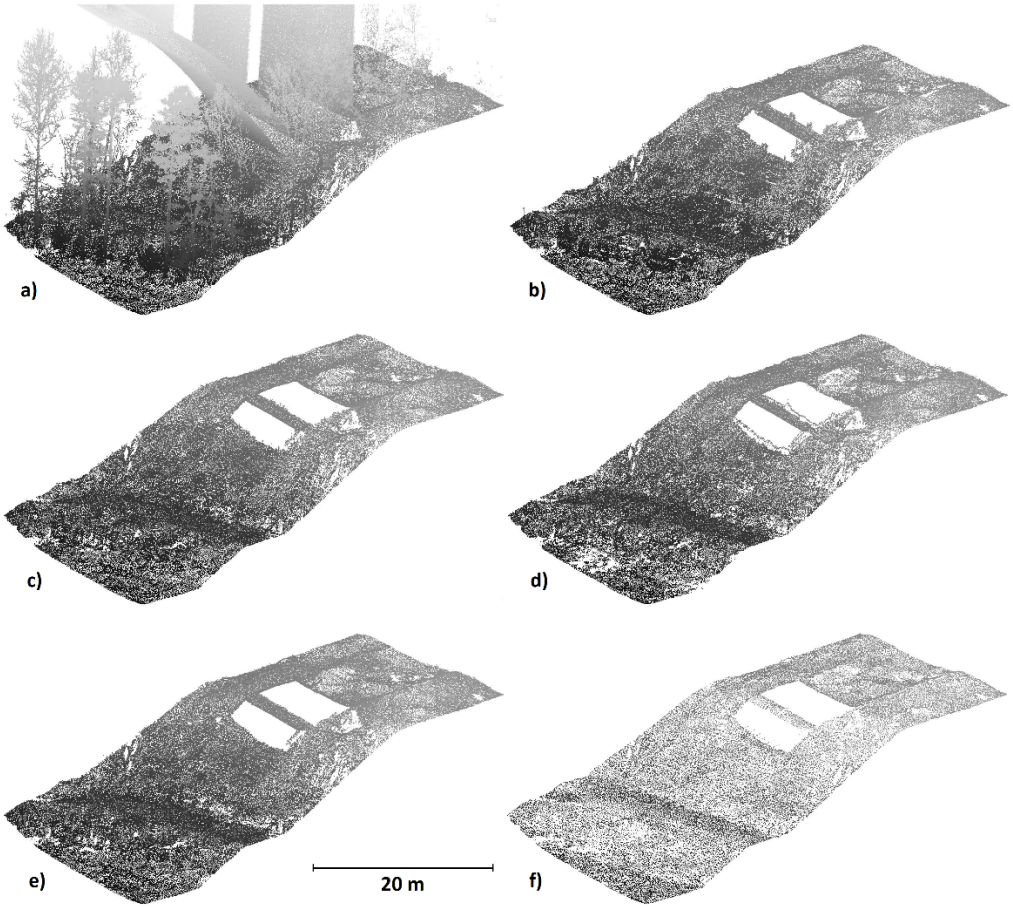

Figure C4. Results of filtering of Site 4 a) original data b) after PMF filtering, c) after SMRF filtering, d) after CSF filtering, e) after ATIN filtering, f) after MVSR filtering.

References

1. Pukanska, K.; Bartos, K.; Hideghety, A.; Kupcikova, K.; Ksenak, L.; Janocko, J.; Gil, M.; Frackiewicz, P. et al.: Hardly Accessible Morphological Structures - Geological Mapping and Accuracy Analysis of SfM and TLS Surveying Technologies. ACTA MONTANISTICA SLOVACA, vol. 25, no. 4, pp. 479 - 493, 2020. ISSN 1335-1788. https://doi.org/10.46544/AMS.v25i4.04.
2. Kalvoda, P.; Nosek, J.; Kuruc, M.; Volařík, T.; Kalvodova, P. Accuracy Evaluation and Comparison of Mobile Laser Scanning and Mobile Photogrammetry Data; IOP Conference Series: Earth and Environmental Science; IOP Publishing Ltd.: Bristol, UK, 2020; pp. 1–10, ISSN 1755-1307. https://doi:10.1088/1755-1315/609/1/012091.
3. Štroner, M.; Urban, R.; Línková, L. A New Method for UAV Lidar Precision Testing Used for the Evaluation of an Affordable DJI ZENMUSE L1 Scanner. Remote Sens. 2021, 13, 4811. https://doi.org/10.3390/rs13234811.
4. Guillaume, A.S.; Leempoel, K.; Rochat, E.; Rogivue, A.; Kasser, M.; Gugerli, F.; Parisod, C.; Joost, S. Multiscale Very High Resolution Topographic Models in Alpine Ecology: Pros and Cons of Airborne LiDAR and Drone-Based Stereo-Photogrammetry Technologies. Remote Sens. 2021, 13, 1588. https://doi.org/10.3390/rs13081588.
5. Jon, J.; Koska, B.; Pospíšil, J. Autonomous Airship Equipped with Multi-Sensor Mapping Platform. ISPRS International Archives of the Photogrammetry. Remote Sens. Spat. Inf. Sci. 2013, 40, 119–124. ISSN 2194-9034, doi:10.5194/isprsarchives-XL-5-W1-119-2013.
6. Berrett, B.E.; Vernon, C.A.; Beckstrand, H.; Pollei, M.; Markert, K.; Franke, K.W.; Hedengren, J.D. Large-Scale Reality Modeling of a University Campus Using Combined UAV and Terrestrial Photogrammetry for Historical Preservation and Practical Use. Drones 2021, 5, 136. https://doi.org/10.3390/drones5040136.
7. McMahon, C.; Mora, O.E.; Starek, M.J. Evaluating the Performance of sUAS Photogrammetry with PPK Positioning for Infrastructure Mapping. Drones 2021, 5, 50. https://doi.org/10.3390/drones5020050.
8. Le Van Canh, X.; Cao Xuan Cuong, X.; Nguyen Quoc Long, X.; Le Thi Thu Ha, X.; Tran Trung Anh, X.; Xuan-Nam Bui, X.: Experimental Investigation on the Performance of DJI Phantom 4 RTK in the PPK Mode for 3D Mapping Open-Pit Mines. Inzynieria Mineralna-Journal of The Polish Mineral Engineering Society, vol. 1, no. 2, pp. 65 - 74, 2020. ISSN 1640-4920. http://doi.org/10.29227/IM-2020-02-10.

9. Fagiewicz, K.; Lowicki, D.: The Dynamics of Landscape Pattern Changes in Mining Areas: The Case Study of The Adamow-Kozmin Lignite Basin. Quaestiones Geographicae, vol. 38, no. 4, pp. 151 - 162, 2019. ISSN 0137-477X. https://doi.org/10.2478/quageo-2019-0046.
10. Zimmerman, T.; Jansen, K.; Miller, J. Analysis of UAS Flight Altitude and Ground Control Point Parameters on DEM Accuracy along a Complex, Developed Coastline. Remote Sens. 2020, 12, 2305. https://doi.org/10.3390/rs12142305.
11. Brunier, G.; Oiry, S.; Gruet, Y.; Dubois, S.F.; Barillé, L. Topographic Analysis of Intertidal Polychaete Reefs (Sabellaria alveolata) at a Very High Spatial Resolution. Remote Sens. 2022, 14, 307. https://doi.org/10.3390/rs14020307.
12. Taddia, Y.; González-García, L.; Zambello, E.; Pellegrinelli, A. Quality Assessment of Photogrammetric Models for Façade and Building Reconstruction Using DJI Phantom 4 RTK. Remote Sens. 2020, 12, 3144. https://doi.org/10.3390/rs12193144.
13. Kavaliauskas, P.; Židanavičius, D.; Jurelionis, A. Geometric Accuracy of 3D Reality Mesh Utilization for BIM-Based Earthwork Quantity Estimation Workflows. ISPRS Int. J. Geo-Inf. 2021, 10, 399. https://doi.org/10.3390/ijgi10060399.
14. Schroder, W.; Murtha, T.; Golden, C.; Scherer, A.K.; Broadbent, E.N.; Almeyda Zambrano, A.M.; Herndon, K.; Griffin, R. UAV LiDAR Survey for Archaeological Documentation in Chiapas, Mexico. Remote Sens. 2021, 13, 4731. https://doi.org/10.3390/rs13234731.
15. Blistan, P.; Kovanic, L.; Patera, M.; Hurcik, T.: Evaluation quality parameters of DEM generated with low-cost UAV photogrammetry and Structure-from-Motion (SfM) approach for topographic surveying of small areas. Acta Montanistica Slovaca, vol. 24, no. 3, pp. 198 - 212, 2019. ISSN 1335-1788.
16. Nesbit, P.R.; Hubbard, S.M.; Hugenholtz, C.H. Direct Georeferencing UAV-SfM in High-Relief Topography: Accuracy Assessment and Alternative Ground Control Strategies Along Steep Inaccessible Rock Slopes. Remote Sens. 2022, 14, 490. https://doi.org/10.3390/rs14030490.
17. Vosselman, G. Slope based filtering of laser altimetry data. Int. Arch. Photogramm. Remote Sens. 2000, 33, 935–942.
18. Sithole, G. Filtering of laser altimetry data using a slope adaptive filter. Int. Arch. Photogramm. Remote Sens. 2001, 34, 203–210.
19. Susaki, J. Adaptive Slope Filtering of Airborne LiDAR Data in Urban Areas for Digital Terrain Model (DTM) Generation. Remote Sens. 2012, 4, 1804-1819. https://doi.org/10.3390/rs4061804.
20. Kraus, K.; Pfeifer, N. Determination of terrain models in wooded areas with airborne laser scanner data. ISPRS J. Photogramm. Remote Sens., vol. 53, no. 4, pp. 193–203, 1998. https://doi.org/10.1016/S0924-2716(98)00009-4.
21. Axelsson, P. DEM generation from laser scanner data using adaptive TIN models. Int. Arch. Photogramm. Remote Sens. 2000, 33, 111–118.
22. Kobler, A.; Pfeifer, N.; Ogrinc, P.; Todorovski, L.; Ostir, K.; Dzeroski, S. Repetitive interpolation: A robust algorithm for DTM generation from Aerial Laser Scanner Data in forested terrain. Remote Sensing of Environment, 108 (1) (2007), pp. 9-23. https://doi.org/10.1016/j.rse.2006.10.013.
23. Zhang, K.; Chen, S.C.; Whitman, D.; Shyu, M.L.; Yan, J.; Zhang, C. A progressive morphological filter for removing nonground measurements from airborne LIDAR data. IEEE Trans. Geosci. Remote Sens. 2003, 41, 872–882. https://doi.org/10.1109/TGRS.2003.810682.
24. Pingel, T.J.; Clarke, K.C.; McBride, W.A. An improved simple morphological filter for the terrain classification of airborne LIDAR data. ISPRS J. Photogramm. Remote Sens, 2013. 77, 21–30. https://doi.org/10.1016/j.isprsjprs.2012.12.002.
25. Li, Y. Filtering Airborne LIDAR Data by AN Improved Morphological Method Based on Multi-Gradient Analysis. ISPRS Int. Arch. Photogramm. Remote Sens. Spat. Inf. Sci. 2013, XL-1/W1, 191–194. https://doi.org/10.5194/isprsarchives-XL-1-W1-191-2013.
26. Im, J.; Jensen, J.R.; Hodgson, M.E. Object-based land cover classification using high-posting-density LiDAR data. GIScience Remote Sens. 2008, 45, 209–228. https://doi.org/10.2747/1548-1603.45.2.209.
27. Zhang, J.; Lin, X.; Ning, X. SVM-Based Classification of Segmented Airborne LiDAR Point Clouds in Urban Areas. Remote Sens. 2013, 5, 3749–3775. https://doi.org/10.3390/rs5083749.
28. Tovari, D.; Pfeifer, N. Segmentation based robust interpolation—A new approach to laser data filtering. Int. Arch. Photogramm. Remote Sens. Spat. Inf. Sci. 2005, 36, 79–84.
29. Vosselman, G.; Coenen, M.; Rottensteiner, F. Contextual segment-based classification of airborne laser scanner data. ISPRS J. Photogramm. Remote Sens. 2017, 128, 354–371. https://doi.org/10.1016/j.isprsjprs.2017.03.010.
30. Bartels, M.; Wei, H. Segmentation of LiDAR data using measures of distribution. Int. Arch. Photogramm., Remote Sens. Spatial Inf. Sci., vol. 36, no. 7, pp. 426–31, 2006.
31. Crosilla, F.; Macorig, D.; Scaioni, M.; Sebastianutti, I.; Visintini, D. LiDAR data filtering and classification by skewness and kurtosis iterative analysis of multiple point cloud data categories. Appl. Geomatics, vol. 5, no. 3, pp. 225–240, 2013. https://doi.org/10.1007/s12518-013-0113-9.
32. Buján, S.; Cordero, M.; Miranda, D. Hybrid Overlap Filter for LiDAR Point Clouds Using Free Software. Remote Sens. 2020, 12, 1051. https://doi.org/10.3390/rs12071051.
33. Zhang, W.; Qi, J.; Wan, P.; Wang, H.; Xie, D.; Wang, X.; Yan, G. An easy-to-use airborne LiDAR data filtering method based on cloth simulation. Remote Sens. 2016, 8, 501. https://doi.org/10.3390/rs8060501.
34. Rizaldy, A.; Persello, C.; Gevaert, C.; Oude Elberink, S.; Vosselman, G. Ground and Multi-Class Classification of Airborne Laser Scanner Point Clouds Using Fully Convolutional Networks. Remote Sens. 2018, 10, 1723. https://doi.org/10.3390/rs10111723.
35. Zhang, J.; Hu, X.; Dai, H.; Qu, S. DEM Extraction from ALS Point Clouds in Forest Areas via Graph Convolution Network. Remote Sens. 2020, 12, 178. https://doi.org/10.3390/rs12010178.

36. Cai, S.; Zhang, W.; Liang, X.; Wan, P.; Qi, J.; Yu, S.; Yan, G.; Shao, J. Filtering Airborne LiDAR Data Through Complementary Cloth Simulation and Progressive TIN Densification Filters. Remote Sens. 2019, 11, 1037. https://doi.org/10.3390/rs11091037.
37. Hu, X.; Yuan, Y. Deep-Learning-Based Classification for DTM Extraction from ALS Point Cloud. Remote Sens. 2016, 8, 730. https://doi.org/10.3390/rs8090730.
38. Jakovljevic, G.; Govedarica, M.; Alvarez-Taboada, F.; Pajic, V. Accuracy Assessment of Deep Learning Based Classification of LiDAR and UAV Points Clouds for DTM Creation and Flood Risk Mapping. Geosciences 2019, 9, 323. https://doi.org/10.3390/geosciences9070323.
39. Yang, Z.; Jiang, W.; Lin, Y.; Elberink, S.O. Using Training Samples Retrieved from a Topographic Map and Unsupervised Segmentation for the Classification of Airborne Laser Scanning Data. Remote Sens. 2020, 12, 877. https://doi.org/10.3390/rs12050877.
40. Li, H.; Ye, W.; Liu, J.; Tan, W.; Pirasteh, S.; Fatholahi, S.N.; Li, J. High-Resolution Terrain Modeling Using Airborne LiDAR Data with Transfer Learning. Remote Sens. 2021, 13, 3448. https://doi.org/10.3390/rs13173448.
41. Na, J.; Xue, K.; Xiong, L.; Tang, G.; Ding, H.; Strobl, J.; Pfeifer, N. UAV-Based Terrain Modeling under Vegetation in the Chinese Loess Plateau: A Deep Learning and Terrain Correction Ensemble Framework. Remote Sens. 2020, 12, 3318. https://doi.org/10.3390/rs12203318.
42. Moudrý, V.; Klápště, P.; Fogl, M.; Gdulová, K.; Barták, V.; Urban, R. Assessment of LiDAR ground filtering algorithms for determining ground surface of non-natural terrain overgrown with forest and steppe vegetation. Measurement 2020, 150. https://doi.org/10.1016/j.measurement.2019.107047.
43. Chen, C.; Guo, J.; Wu, H.; Li, Y.; Shi, B. Performance Comparison of Filtering Algorithms for High-Density Airborne LiDAR Point Clouds over Complex LandScapes. Remote Sens. 2021, 13, 2663. https://doi.org/10.3390/rs13142663.
44. Klápště, P.; Fogl, M.; Barták, V.; Gdulová, K.; Urban, R.; Moudrý, V. Sensitivity analysis of parameters and contrasting performance of ground filtering algorithms with UAV photogrammetry-based and LiDAR point clouds. Int. J. Digit. Earth 2020, 13,1672–1694, https://doi.org/10.1080/17538947.2020.1791267.
45. Štroner, M.; Urban, R.; Lidmila, M.; Kolář, V.; Křemen, T. Vegetation Filtering of a Steep Rugged Terrain: The Performance of Standard Algorithms and a Newly Proposed Workflow on an Example of a Railway Ledge. Remote Sens. 2021, 13, 3050. https://doi.org/10.3390/rs13153050.
46. Wang, Y.; Koo, K.: Vegetation Removal on 3D Point Cloud Reconstruction of Cut-Slopes Using U-Net. APPLIED SCIENCES-BASEL, vol. 12, no. 1, 2022. https://doi.org/10.3390/app12010395.
47. Mohamad, N.; Ahmad, A.; Khanan, M.; Din, A.: Surface Elevation Changes Estimation Underneath Mangrove Canopy Using SNERL Filtering Algorithm and DoD Technique on UAV-Derived DSM Data. ISPRS International Journal of Geo-Information, vol. 11, no. 1, 2022. https://doi.org/10.3390/ijgi11010032.
48. Hui, Z.; Jin, S.; Xia, Y.; Nie, Y.; Xie, X.; Li, N. A mean shift segmentation morphological filter for airborne LiDAR DTM extraction under forest canopy. Optics & Laser Technology, Volume 136, 2021, 106728. https://doi.org/10.1016/j.optlastec.2020.106728.
49. Štular, B.; Lozić, E. Comparison of Filters for Archaeology-Specific Ground Extraction from Airborne LiDAR Point Clouds. Remote Sens. 2020, 12, 3025. https://doi.org/10.3390/rs12183025.